Absolute X-Ray Yields From Laser-Irradiated Ge-Doped Low-Density Aerogels

K. B. Fournier, J. H. Satcher, M. J. May, J. F. Poco, C. M. Sorce, J. D. Colvin, S. B. Hansen, S. A. MacLaren, S. J. Moon, J. F. Davis, F. Girard, B. Villette, M. Primout, D. Babonneau, C. A. Coverdale, D. E. Beutler

February 27, 2009

Disclaimer

This document was prepared as an account of work sponsored by an agency of the United States government. Neither the United States government nor Lawrence Livermore National Security, LLC, nor any of their employees makes any warranty, expressed or implied, or assumes any legal liability or responsibility for the accuracy, completeness, or usefulness of any information, apparatus, product, or process disclosed, or represents that its use would not infringe privately owned rights. Reference herein to any specific commercial product, process, or service by trade name, trademark, manufacturer, or otherwise does not necessarily constitute or imply its endorsement, recommendation, or favoring by the United States government or Lawrence Livermore National Security, LLC. The views and opinions of authors expressed herein do not necessarily state or reflect those of the United States government or Lawrence Livermore National Security, LLC, and shall not be used for advertising or product endorsement purposes.

Absolute X-Ray Yields From Laser-Irradiated Ge-Doped Low-Density Aerogels

K. B. Fournier,* J. H. Satcher, M. J. May, J. F. Poco, C. M. Sorce, J.
D. Colvin, S. B. Hansen,[†] S. A. MacLaren, S. J. Moon, and J. F. Davis[‡]
Lawrence Livermore National Laboratory, Livermore, CA, USA

F. Girard,[§] B. Villette,[¶] M. Primout, and D. Babonneau
*Commissariat à l'Energie Atomique-Direction des Application Militaires (CEA/DAM)
Ile-de-France, F91297 Arpajon, France*

C. A. Coverdale** and D. E. Beutler
Sandia National Laboratory, Albuquerque, NM, USA
(Dated: February 19, 2009)

We have used the OMEGA laser (Laboratory for Laser Energetics, University of Rochester) to measure the X-ray yields from laser-irradiated germanium-doped ultra-low-density aerogel plasmas in the energy range from sub-keV to $\approx$ 15 keV. We have studied the targets' X-ray yields with variation in target size, aerogel density, laser pulse length and laser intensity. For targets that result in plasmas with electron densities in the range of $\approx$ 10% of the critical density for 3ω light, one can expect 10–11 J/sr of X-rays with energies above 9 keV, and 600–800 J/sr for energies below 3.5 keV. In addition to the X-ray spectral yields, we have measured the X-ray temporal waveforms and found that the emitted X rays generally follow the delivered laser power, with late-time enhancements of emitted X-ray power correlated with hydrodynamic compression of the hot plasma. Also, we find the laser energy reflected from the target by plasma instabilities to be 2–7% of the incident energy for individual beam intensities $\approx 10^{14}$–10^{15} W/cm^2. We also have characterized the propagation of the laser heating in the target volume with two-dimensional imaging. We find the source-region heating to be correlated with the temporal profile of the emitted X-ray power.

PACS numbers: Valid PACS appear here

I. INTRODUCTION

Bright, multi-keV X-ray sources are essential for radiography of high-energy-density physics experiments [1, 2], including those supporting inertial-confinement fusion (ICF) research, as well as applications such as materials testing. In this context, there are two parameters of importance: the energy of the emitted photons, which determines how penetrating the X rays are for radiographic purposes, and the brightness of the source, which determines the ability of a radiograph to detect small features. ICF experiments, such as those that will be carried out at the National Ignition Facility at Lawrence Livermore National Laboratory (LLNL) [3, 4] and at the French Commissariat à l'Energie Atomique's (CEA) Laser MegaJoule [5], will require brighter, harder-photon spectra [6] than were previously available.

For a given laser energy to drive multi-kilo-electron volt (keV) X-ray-backlight sources, the only way for the source to get brighter is for it to convert the laser to X rays more efficiently. However, as the photon energy of the X-ray spectrum increases, the efficiency of the X-ray emitter drops sharply for solid targets [7, 8]. Underdense sources, where the electron density is less than 20% of the laser's critical density ($n_e/n_{cr} < 0.2$), have been shown to be inherently more efficient at laser-energy-to-X-ray conversion than traditional solid-foil backlighter targets [9–12], e.g. 10's of percent for gas targets [9, 10] versus less than 1% for solid targets in the same photon range [7, 9]. This is because the underdense nature of the target allows the laser to burn through the target supersonically [13]. Thus the laser heats the target volumetrically, achieving high temperatures and ionizing the X-ray emitting ions without expending a lot of energy on hydrodynamic motion of bulk material [11].

In recent years, ultra-low-density targets for X-ray generation by nanosecond-class lasers have been demonstrated [9, 10]. These targets were noble gasses (Ar, Kr, Xe) confined in low-mass enclosures. In the case of L-shell Kr radiation (X-ray energies $h\nu \approx 1.6$ keV), conversion of up to 35% of the laser energy has been demonstrated [10], L-shell Xe radiation ($h\nu \approx 4.5$ keV) has a measured conversion efficiency (CE) of $\approx$ 10%. More recently, laser targets that are solid at room temperature, but which have densities that are equivalent to those of the gaseous targets, have been demonstrated as efficient X-ray sources [12], with $\approx$ 2% CE for $h\nu \approx 4.7$ keV. These targets were ultra-low-density ($\rho = 3 - 4$ mg/cm^3)

---

*Electronic address: fournier2@llnl.gov
[†]Permanent address Sandia National Laboratories, Albuquerque, NM, USA
[‡]Also at Alme & Associates, 6020 Richmond Highway, Alexandria, Virginia 22303; Electronic address: JDavis@aol.com
[§]Electronic address: frederic.girard@cea.fr
[¶]Electronic address: bruno.villette@cea.fr
**Electronic address: cacover@sandia.gov

silicon-dioxide (SiO$_2$) aerogels [14] that contain a trace amount of a high-Z dopant, Ti (Z=24) in the case of [12], that is the source of the desired X-ray emission lines [15]. The same supersonic laser-heating propagation that leads to efficient production of a volumetric, high-temperature plasma in the gas targets was confirmed to take place in the doped aerogel targets [16]. Recent work has measured the laser-to-X-ray CE of nanostructured titanium-dioxide materials [17], with results of 3.7% CE in a spectral band centered on 4.7 keV. Researchers have also recently had success efficiently making multi-keV X rays from pre-exploded foils [18, 19], in which an early laser pulse makes an expanded, underdense cloud of hot material that is then heated to produce X rays by the main (delayed) laser pulse. These targets have resulted in a record CE for a solid target of 9% in the 4.7 keV band [19].

Part of the present research has been to find materials that are solid at room temperature, can be shaped and handled easily, and are efficient producers of high-energy X rays. Our work in Ref. [12] used titanium at a concentration of 3 atomic percent (at%) as the aerogel dopant that produced the X rays. At that time, 3 at% seemed to be the maximum concentration achievable. The experiments described here used low-density, germanium-doped (Ge, Z=32) aerogel as the converter material. This target is a significant advance in both the chemistry of aerogel materials and in the fabrication of laser-driven X-ray sources. We can routinely achieve up to 20 at% Ge with aggregate target densities below 3.0 mg/cm^3. The following sections present our experimental set-up, the targets that produced the X-ray sources, and analysis of data collected from these targets. We find that our low-density aerogel targets convert $\approx$ 0.7% of the laser's energy into X rays between 9.0 and 15 keV. With a large contribution of continuum emission below 10 keV, the average spectral energy emitted from the source is $\approx$ 7.1 keV, and $\gtrsim$ 30% of the laser's energy is converted into X-rays with energy >1 keV. This work represents an experimental optimization of the performance of doped-aerogel X-ray sources and supersedes results previously published in [20].

II. EXPERIMENTAL ARRANGEMENT

A. The OMEGA Laser

The OMEGA laser (Laboratory for Laser Energetics, University of Rochester) is a 60 beam Nd:glass laser that can deliver up to 30 kJ of 3ω (λ=0.351 μm) light to the target chamber center [21, 22]. Only forty of the 60 OMEGA beams were used in the present experiments, the cylindrical shape of the Be tubes that held the aerogel blocked beams that came from directions near-to-normal to the cylindrical axis. The distribution of beams around the OMEGA chamber results in rings of beams, or beam cones, at three distinct angles (21.42, 42.00 and 58.85°,
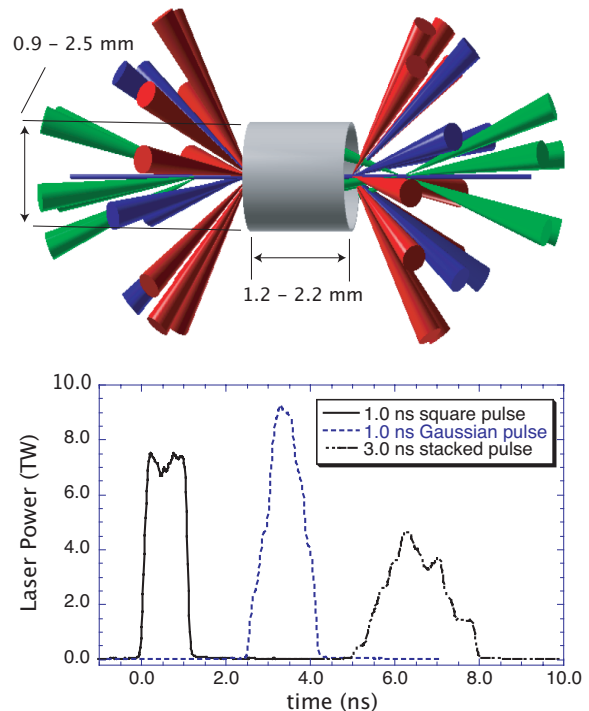

FIG. 1: (top) OMEGA beam cones and cylindrical target and (bottom) three of the laser power profiles used to drive the aerogel targets (shown with arbitrary offsets for clarity).

cones 1, 2 and 3, respectively) for the orientation of our cylindrical targets, which are shown in Fig. 1. Note, the two steeper cones of beams are focused at the open faces of the targets, the best-focus position of the cone 1 beams is offset by 1100 μm and diverges onto the face of the target. The two open faces of the cylinders were each irradiated with up to 10 kJ of ultraviolet (0.351 μm) laser light.

The best focus available for each beam is a spot approximately 60 μm in diameter, but can be made larger as required by changing the beam's lens position. Several techniques exist for smoothing the intensity distribution across the laser spot, including inserting phase plates in the focusing optics, adding spectral noise to the seed pulse, and separating, then overlapping, the different polarization components in the beam (distributed polarization rotators or DPRs). It is this latter method that we used in the present experiments. The use of the DPRs means that the individual beam footprints are nearly 80 μm diameter at best focus in the plane of the beam. Note, the effect of the individual beam-cone angles on the laser spot is to elongate it one direction by the inverse of the cosine of the angle. This effect is taken into account in computing the laser intensity on the target by modeling the laser spot as an ellipse. Three laser irradiation conditions were used in the present experiments: tight, moderate and wide focus configuration, which are defined in Table I. The variations of target yield with

description	cone	spot dimensions (μm $\times$ μm)	typical intensity (W/cm^2)
tight	1	77 $\times$ 83	
	2	155 $\times$ 208	6$\times10^{16}$
	3	165 $\times$ 319	
moderate	1	363 $\times$ 390	
	2	363 $\times$ 404	2–8$\times10^{15}$
	3	363 $\times$ 580	
– or –	1	563 $\times$ 605	
	2	800 $\times$ 1077	
	3	500 $\times$ 967	
wide	1	463 $\times$ 498	
	2	1100 $\times$ 1481	0.6–2$\times10^{15}$
	3	775 $\times$ 1498	

TABLE I: The spot dimensions for the three focus conditions used in the present experiments for the cone 1 (21.42°), cone 2 (42.02°) and cone 3 (58.85°) beams on the P5-P8 axis. The quoted dimensions are the minor and major axes of the elliptical beam spots at the face of the target.

respect to laser focusing and laser-power pulse width are discussed in Section III.

Laser-power pulse shapes can be tailored to deliver the power in flattop pulses or pulses with rising or falling ramps. Typically, pulse lengths range from one to three nanoseconds. Individual beams can be delayed relative to others by arbitrary amounts up to 6 ns. The X-ray targets in the present work were irradiated with three different power profiles: one that had all the beams incident simultaneously with a 1-ns square pulse shape (pulse shape SG1018), one with small delays added to individual beams to make a 1.0–1.2-ns-wide Gaussian pulse shape, and one where the beams were fired in three groups with delays added, from earliest to latest for cones 3, 2, and 1, respectively, over a 3-ns interval. The three laser-power waveforms as delivered to *one* face of the doped-aerogel target, measured by facility diagnostics during these experiments, are shown in Fig. 1.

B.   The Target

The X-ray source in these experiments was a germanium-doped SiO$_2$ aerogel that contained 50% Ge by weight (20 atomic percent). Details about the sol-gel chemistry and aerogel formation process are given in Ref. [14, 15]. The aerogels as fielded were made at four densities, 3.3, 3.6, 4.8 and 6.5 mg/cm^3. These densities resulted in plasmas with electron densities $10-20\%$ of the laser's critical density, n_{cr}=1.1$\times10^{21}/\lambda^2$, where λ is the laser's wavelength in μm. The critical density is $\approx 9\times10^{21}$ cm^{-3} for $\lambda = 0.351$ μm light. We compute the electron density in the X-ray emitting plasmas that are

formed from the aerogel targets as

$$n_e = \frac{N_A \rho <z>}{<A>} \quad (1)$$

where N_A is Avagadro's number, ρ is the target density in g/cm^3, and the average ion charge $<z>$ and average atomic mass $<A>$ are given by $<A>=f_{Si}A_{Si} + f_O A_O + f_{Ge}A_{Ge}$ and $<z>=f_{Si}z_{Si} + f_O z_O + f_{Ge}z_{Ge}$, where f_Z is the molar fraction of element Z in the aerogel (0.13, 0.67 and 0.20 for Si, O and Ge, respectively), A_Z is the molar mass of element Z, and z_Z is the ion charge on element Z (assumed to be 13, 8, and 30 for Si, O and Ge, respectively, based on the measured spectral data described below and nonlocal thermodynamic equilibrium calculations of the plasma ionization balance [23]). The 15% critical-density value for these targets (ρ=4.8 mg/cm^3) was chosen as the initial target design based on experience with X-ray output from gas targets [10, 11] that showed a peak in the conversion efficiency for Kr L-shell X rays at $n_e/n_{cr} \approx$0.15. These aerogel targets are seen to have higher X-ray yields at lower electron densities (as is discussed in Section III). The higher level of dopant possible in these targets compared to previous Ti-doped aerogels [12] is due to the chemical similarity of Ge and Si. Unlike the case of the Ti dopant, where the Ti atoms are suspended and supported in the SiO$_2$ matrix, the Ge atoms of the present targets are incorporated directly into the aerogel polymer chains.

The Ge-doped aerogel material was cast in 75-μm thick Be cylinders that ranged from 1.2 to 2.2 mm in length and had inner diameters (IDs) from 0.9 to 2.5 mm (see Fig. 1). The Be walls of the cylinders transmit greater than 99% of the $>$ 10 keV X rays that were the subject of these investigations.

Inspection of the aerogel targets showed no shrinkage of the aerogel material in the cylinders that would lead to densification. The material was completely transparent and without any visible defects suggesting that the Ge dopant remained uniformly dispersed throughout the target volume. Final aerogel densities were determined by gravimetric analysis of witness pieces made at the same time as the laser targets. The final Ge concentration in the aerogels after polymerization and solvent extraction was determined by inductively coupled plasma optical emission spectroscopy (ICP-OES) measurements of witness pieces, the accuracy of the technique is quoted as $\pm$ 10% [24, 25]. Analysis of two different preparations of aerogels both yielded a value of 20.8 atomic percent of Ge. From transmission electron micrograph (TEM) imaging, the microstructure of the aerogel materials consists of a network of nanometer-sized particles. Based on these images, the void sizes for a fractured surface in the final aerogels are distributed in the hundreds-of-nanometers range.

C. Spectral Diagnostics

1. Time-integrated X-ray spectra

X-ray yields from the laser-heated aerogel targets were measured with a number of independently calibrated photometric detectors. One instrument, the HENWAY four-channel crystal spectrometer [26] recorded time-integrated X-ray spectral yields in both hard ($4.5 \leq h\nu \leq 15$) and soft ($1 \leq h\nu \leq 3$) bands from every Ge-doped aerogel target. The HENWAY spectrometer had a view of one face of the target at an angle of 61° with respect to the target axis. Two channels gave coverage in the stated energy bands: the higher-energy channel used a pentaerythritol (PET) crystal, while the lower-energy channel was measured with a potassium-hydrogen-phthalate (KAP) crystal. The spectra from the KAP-crystal channel provide ambiguous data with multiple orders of lines appearing in each spectrum. The PET-crystal measured the spectrum between 4.5–15 keV. This channel was filtered differently across the face of the crystal: 25 or 75 μm Be, plus either 6 or 12-μm Al, and strips of 25-μm V, 25.4-μm Cu or 45.7 μm Ge foils; on some shots, 12.7 μm of Fe was added across the whole face of the crystal. Absorption edges from the filter foils serve as energy fiducials allowing calibration of the positions of measured lines. The spectra were recorded on Kodak DEF film. The known response of the film, crystal reflectivity and filter transmission combine to give the spectral yields determined with the PET-crystal channel an accuracy of ± 25–30%.

2. Time-resolved X-ray yields

Three time-resolved diagnostics measured the X-ray power from the laser-driven aerogel targets. One of which was a nine-channel array of photoconductive devices (PCDs) [27] provided by Sandia National Laboratories (SNL). Several of the PCDs have been used for years in radiation-effects experiments on the SNL Z facility, and their responses are well known. The PCDs were filtered with 8 to 254 μm of Kapton in order to discriminate contributions to the output from different regions of the radiated spectrum. Three of the PCDs were filtered with 254 μm of Kapton and an additional 15.6 μm of aluminum. These channels measured X rays above 4 keV, which is complementary with the spectral range measured by the high-energy channel of the HENWAY spectrometer. The PCD array had the same 61° view of the target that the HENWAY spectrometer did. This means that for channels in the array that were supposed to be sensitive to softer X rays, the 75 μm-thick Be wall of the cylinder that holds the aerogel strongly effected the signal, and the array's field of view included both the unattenuated emission from the irradiated face of the cylinder and modified emission through the cylinder wall. The PCD signals were recorded with Tektronix TDS6804 oscilloscopes (50-ps sampling), and redundant traces were read on TDS694C oscilloscopes. The signals were sent to the scopes down 60 ft of 3/8" heliax cable; bandwidth loss in the cables, which was significant, was quantified before the shots. All diagnostic information from the PCDs is frequency compensated according to the known bandwidth losses, and corrected for the PCD dc-bias response at large voltage responses. The PCD-measured yields are considered accurate to 20–25%.

Two diagnostics provided complimentary measurements of yield in the X-ray range below 4 keV, they are the CEA's DMX [28] and LLNL's DANTE [29] arrays. The DMX [28] is a broadband, time-resolved X-ray diode array that measures X-ray power over the whole emitted spectrum from $\lesssim$ 0.1 keV to 20 keV, with five channels covering the heliumlike and hydrogenlike germanium lines in the spectral region of 9–15 keV. The spectral range of each channel was adjusted by choosing appropriate filter materials. Hard X-ray yield values are assessed from the DMX data for two spectral ranges: between 4 and 6 keV, and for energies above 4 keV up to 20 keV. Comparisons with the HENWAY spectral fluence in the 9–15 keV energy region agree to better than 10% with DMX measurements. The overall relative uncertainty for DMX-measured X-ray yields is ±20% considering the filter transmission and detector sensitivity calibrations and the unfold treatment necessary to take into account the broadband response of the DMX channels.

DANTE [29] is a 13 channel X-ray diode (XRD) array, which also had different filtration on each channel used. The first 11 DANTE channels are designed to provide finely resolved coverage from 100 eV to 3 keV, the time resolved signals are integrated to give the total X-ray energy through the filters. The differential signals (after correcting for filter transmission and diode response) are then used to reconstruct the source spectrum. Details on the data-fitting method for spectral reconstruction are given in [30]. The DANTE signals from < 300 eV to approximately 3.5 keV provide the low-energy spectral data that overlap with the DMX measurements and that augment the HENWAY PET channel spectral data.

The DANTE and the DMX have symmetric views of the target that are at 37.4° to the target axis. Thus, the DANTE and DMX see much more of the irradiated face of the target than do HENWAY or the SNL PCDs, and give a more reliable measurements of the soft X-ray part of the target's output than do HENWAY or the SNL PCDs. The data obtained with the DMX and DANTE instruments are in good agreement over their common spectral range, which is < 3 keV. These are the data that are reduced to produce the soft X-ray yield results in § III A 3 (Table III).
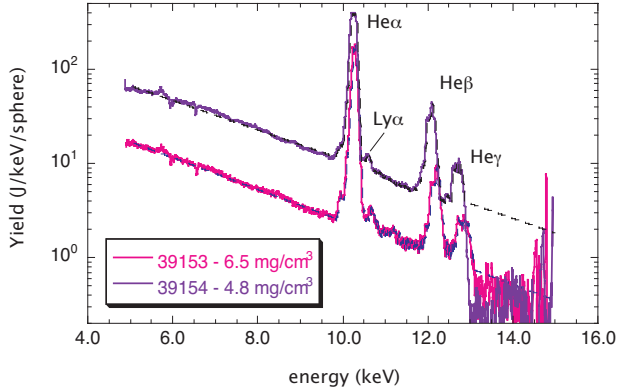
FIG. 2: Two spectra from Ge-doped (20 at%) aerogel targets measured with the HENWAY spectrometer. Shown are both reduced spectral data (solid lines) and continuum fits (dashes). The target for shot 39154 had density 4.8 mg/cm^3, and for shot 39153, 6.5 mg/cm^3. The laser intensity on target ranged from 6.2–6.6×10^{16} W/cm^2.

III. RESULTS

A. X-Ray Spectral Results

1. Time-integrated X-ray spectra

The measured X-ray spectra from two laser-heated doped-aerogel targets are shown in Fig. 2. Both the raw data from the HENWAY PET-crystal channel, and a fit to the continuum regions are shown. The spectra are dominated by the He$_\alpha$ ($1s^2 - 1s2p$) line of Ge^{30+} at 10.3 keV, with He$_\beta$ ($1s^2 - 1s3p$) and He$_\gamma$ ($1s^2 - 1s4p$) features are also visible above 12 keV. The H-like Ly$_\alpha$ line ($1s - 2p$) is also visible in Fig. 2 at $\approx$ 10.6 keV. The continuum emission on the soft side of each measured spectrum accounts for > 60% of the total emission in the 4.0–15 keV spectral band.

The continuum emission measured in each HENWAY spectrum can be fit to an exponential form to get a time-averaged approximate plasma-electron temperature [30]. Results for the targets in the present work averaged 2.6 keV for shots with tight laser focusing ($I_L \approx 6$×10^{16} W/cm^2), 2.4 keV for shots with moderate laser focusing ($I_L \approx 2$×10^{15} W/cm^2), and 2.1 keV for shots with broad laser focusing ($I_L \approx 6$×10^{14} W/cm^2). The relative intensities of the Ge^{31+} Ly$_\alpha$ to Ge^{30+} He$_\alpha$ line features in Fig. 2, both of which were shot with the tight laser focusing, also suggest temperatures in the target plasmas of 2.5–3.5 keV.

2. Diagnostic consistency and target-yield variation

Three time-resolved diagnostics measured the X-ray power from the laser-driven aerogel targets. All three time-resolved diagnostics were never fielded together on any one shot. When comparisons are made between the HENWAY spectral yields over a limited energy range around the Ge^{30+} He$_\alpha$ feature and the time-integrated signals from these other diagnostics, agreement in the X-ray yields is typically 10–20%. Two examples of the agreement between the HENWAY and PCD measured yields for two sets of Ge-doped aerogel-target shots are shown in Fig. 3. For the data in the top panel of Fig. 3, which compares yields for moderate-density ($\rho = 4.8$ mg/cm^3) and high-density ($\rho = 6.5$ mg/cm^3) targets, all shot with a tight laser focus ($I_L \approx 6$×10^{16} W/cm^2), the agreement between the SNL PCDs and the HENWAY data is quite close, and well within the error bars for both diagnostics. The HENWAY signals have had the fitted continuum extrapolated to 4 keV in order to have a truly accurate comparison. The consistency between identical targets on nominally identical shots is good for the two higher-density targets, and good, but with more variation for the four lower-density targets, which also demonstrate on average a greater X-ray yield.

The lower panel in Fig. 3 shows the X-ray yields in the 4–15 keV band from a set of low-density (ρ=3.2–4.1 mg/cm^3) targets, shot with a moderate laser focus ($I_L \approx 2.5$×10^{15} W/cm^2), that differed in initial target volume (6.9 mm^3 versus 10.8 mm^3). For the seven smaller targets, the two diagnostics agree within the instrumental error bars, with the HENWAY yields being systematically higher than the SNL PCD measurements. Overall, the reproducibility in the yields of these seven targets is quite good. For $\approx$ 19 kJ of laser drive, one can expect 21.8±5.5 J/sr of X-rays in the 4–15 keV band to be emitted, where the uncertainty is the standard deviation of the yields for the set of targets displayed in the lower panel of Fig. 3. The yields for the three larger targets measured with the two diagnostics also agree within the experimental uncertainties, and are not statistically different from the measured yields for the smaller targets, giving 24.2±3.0 J/sr in the 4–15 keV band. One of the purposes in this shot day was to compare the yields of the targets with volumes of 6.9 mm^3 and 10.8 mm^3, with the hypothesis being that the larger targets would emit a proportionately greater yield. This was not seen to be the case. However, the aerogel densities in the smaller targets were higher than those in the larger targets, which may have had a compensating effect.

A comparison of the HENWAY and DMX-measured Ge K-shell yields (9–15 keV band) is shown in the upper panel of Fig. 4. The reduction of the DMX data puts the measured flux into a single effective line and a continuum for this spectral band. Again, the consistency between the two diagnostics is excellent, except for the last data point, shot number 42755, which had a smaller volume (2.1 mm^3) than all the other targets (volume 6.9 mm^3)
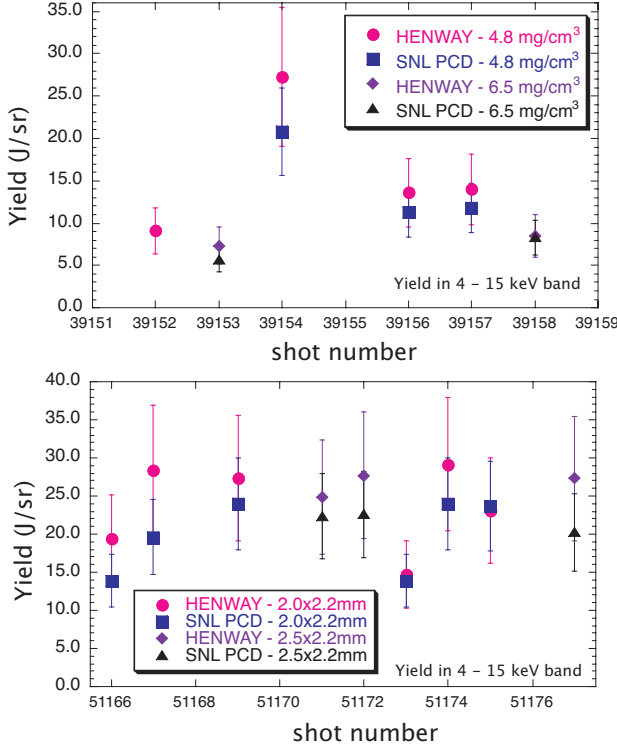
FIG. 3: (top) X-ray yields for the 4–15 keV band from HEN-WAY spectra, and from the high-energy signals from the SNL PCDs, which reflect yields generally above 4 keV, from a series of shots looking at targets with different aerogel densities. (bottom) X-ray yields for the 4–15 keV band from HEN-WAY spectra, and from the high-energy signals from the SNL PCDs, from a series of shots comparing targets of different volumes.
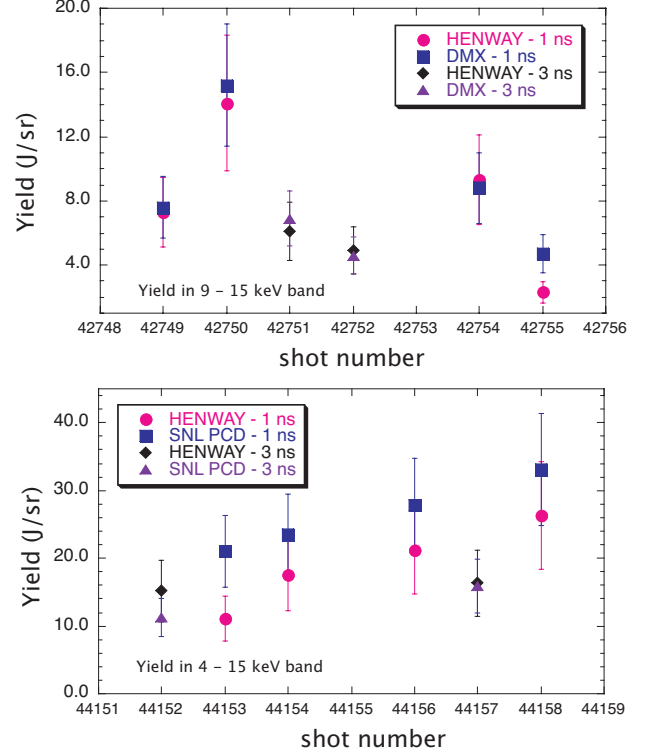
FIG. 4: (top) X-ray yield numbers for the Ge K-shell (9–15 keV) band from HENWAY and from high-energy signals from the DMX, and (bottom) X-ray yield numbers for the 4–15 keV band from HENWAY and the high-energy signals from the SNL PCDs. The principal variation in both sets of shots is the laser pulse length, 1 ns versus 3 ns.

and a correspondingly lower yield. The data points in the upper panel of Fig. 4 contrast the yields from low to moderate-density (ρ = 3.5 or 4.6 mg/cm^3) targets shot with 1 or 3 ns laser irradiations (see Fig. 1). In general, the 3 ns shots produced lower X-ray yields than did the 1 ns shots. The temporal waveforms of the X-ray power is discussed in § III B. The lower panel of Fig. 4 compares the X-ray yields in the 4–15 keV range as measured by HENWAY and the SNL PCDs for a series of shots that kept the aerogel density (ρ=3.7 mg/cm^3) and volume (6.9 mm^3) constant. The targets were irradiated with either 1 ns laser pulses ($I_L \approx 2.0 \times 10^{15}$ W/cm^2) or 3 ns laser pulses ($I_L \approx 2.6 \times 10^{15}$ W/cm^2). Again, the 3 ns shots produced lower X-ray fluences than did the 1 ns shots. Also noteworthy is the observation that both diagnostics recorded an increasing trend in the yields as the day went on, and, unlike the data in Fig. 3, the agreement between the HENWAY and SNL PCD diagnostics is less robust.

In the softer X-ray band below photon energies of 3.5 keV, the agreement between the DANTE and DMX

diagnostics is excellent, as can be seen in Fig. 5. The data in Fig. 5 are from the same set of shots shown in the upper panel of Fig. 4. Each target type and/or shot configuration in this data set is unique, so shot-to-shot variation in the displayed data indicates nothing about target-yield reproducibility. The DANTE spectrum for each shot below 3.5 keV can be smoothly joined to the extrapolated fit to the measured HENWAY continuum from the higher-energy channel, an example of such a treatment is shown in Fig. 6. The DMX is a broad-band instrument, so the lines shown in the figure cannot be obtained directly from DMX signals, but correspond to a fit of energies measured in multiple bands that is translated into a theoretical spectrum. One can see the qualitative agreement in the DMX reconstruction of both the lower-energy and higher-energy line emission with the DANTE reconstruction of the lower-energy line emission and the HENWAY-measured higher-energy line emission. The area of greatest uncertainty, and the spectral region with the least optimization of coverage in the DMX configuration, is how flux is distributed in the 4–9 keV continuum region. Further details on the diagnostics and re-
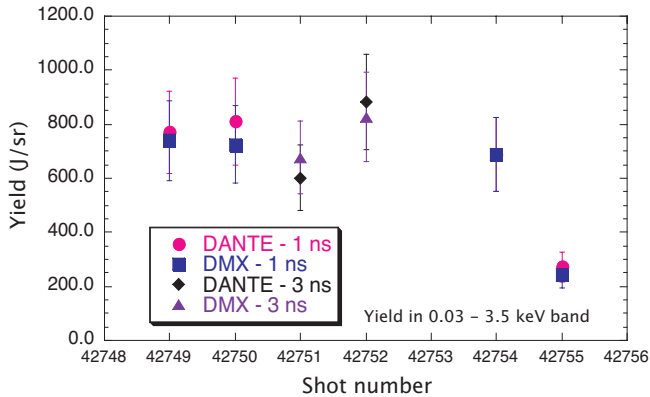
FIG. 5: X-ray yield numbers for the Ge L-shell plus Si K-shell (0.03–3.5 keV) band from the DMX and DANTE diagnostics (the two points for shot 42754 are on top of each other).
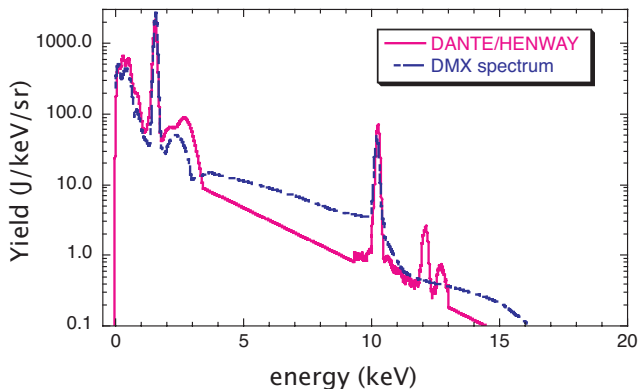

FIG. 6: Comparison of the combined DANTE and HEN-WAY spectral data and the DMX-measured spectrum for shot 42750. This was a typical target in these experiments, with $\rho \approx 3.5$ mg/cm^3, 2.0×2.2 mm (ID×L) cylinder, $I_L \approx 2.0 \times 10^{15}$ W/cm^2, and is the highest-yielding shot in the 9–15 keV band that was obtained.

duction/analysis of hard- and soft-spectral data are given in [30]. In general, one can expect on the order of 45% laser-to-X-ray conversion in the 0.03–3.5 keV band from the typical targets ($\rho \approx 3.7$ mg/cm^3, volume = 6.9 or 10.1 mm^3) shot in these experiments. This large value is consistent with results for L-band emission from Kr gas targets of comparable volume [10]. Averaging over the measured 0.03–3.5 keV X-ray yields from the highest-yielding type of target (1 ns pulse, volume 10.1 mm^3), one can expect 693.8±175 J/sr in the soft X-ray band, where the uncertainty represents both DANTE and DMX instrumental uncertainty and statistical variation in target yields.

3. Target-type summary: variation with density, size, and intensity

In what follows, we summarize the measured X-ray output from a number of different target and laser configurations. Our results in the 9–15 keV spectral band are presented in Figure 7, with the displayed data values and uncertainties listed in Table II. The error bars in the figure are the uncertainties listed in the tables. The data in Fig. 7 (Table II) are averaged for all shots from a class of targets from X-ray spectral measurements made with the HENWAY crystal spectrometer and the DMX. These data are for X-ray emission from K-shell (He- and H-like) Ge ions. The displayed (reported) data are in units of J/sr, although the emission at these energies is isotropic into all solid angles. The uncertainty associated with each point is the square root of the quadrature sum of the standard deviation in the whole set of measurements for each target type and the uncertainty in the response of each instrument (25% for the HENWAY, 20% for the DMX). Also listed in Table II are the yields from these targets in J/sr in the spectral range between 4–15 keV. These yields have been estimated by fitting an exponential slope to smoothed data on the HENWAY film that remained after a background subtraction [30], and averaged with the yields from the SNL PCDs (known to 20–25%) when available. We find a yield of 10.1±3.5 J/sr for X-rays with energies above 9 keV, averaging over type 1, 2 and 3 targets, or, equivalently, 127±44 J/sphere assuming isotropic emission.

Our results in the 0.03–3.5 keV spectral band are presented in Figure 8, with the displayed data values and uncertainties listed in Table III. The data in Fig. 8 (Table III) are averaged from the de-convolved X-ray signals from the DANTE and DMX diagnostics. These data for the spectral range below 3.5 keV are given as yield per steradian. The DANTE and DMX diagnostics had equivalent views of the X-ray source that (largely) avoided complications of X-ray attenuation through the targets' walls. Emission in this soft X-ray range includes X rays from L-shell Ge ions and emission from K-shell Si ions that are present in the SiO$_2$ aerogel. The error bars for the data in Fig. 8 (Table III) are also the quadrature sum of the standard deviation in the whole set of measurements for each target type and the uncertainty in the response of each instrument, both ±20%. We find a yield of 678±157 J/sr from our targets for energies below 3.5 keV for 1 ns laser pulses, averaging over the type 2 and 3 targets only.

Overall, the statistical variation in the yield from a given target type does not follow a clear trend. In general, except for the case of the second and fifth points in both Figs. 7 and 8, the statistical variation in the measured hard and soft X-ray yields for a given type of target are less than ±25% around the average value for that class of target, and generally less than ±10% for the soft X-ray band. In the case of the second point in Figs. 7 and 8 (blue square), which is for targets with aerogel densities
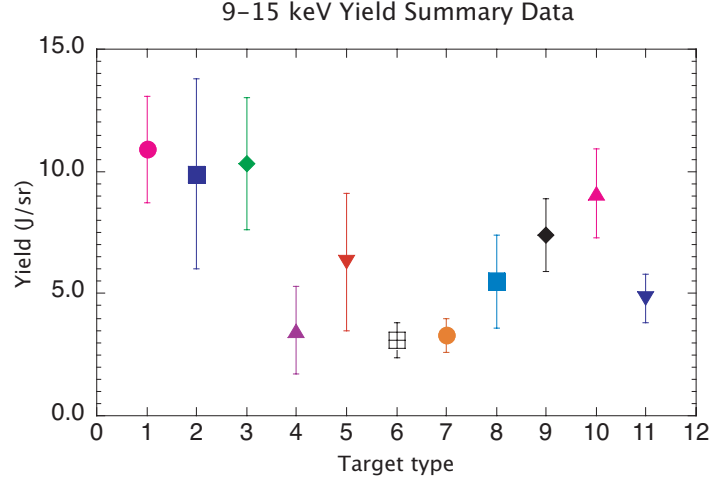
FIG. 7: Yield data summary (in J/sr) for Ge-doped aerogels in the 9–15 keV band. The symbols in the figure represent the target types described in Table II, with the symbols from left to right corresponding to the entries going down the table.

Type	ρ (mg/cm^3)	n_e/n_{cr}	target size (mm×mm)	pulse length (ns)	focus	I_L (W/cm^2)	Yield [9-15 keV] (J/sr)	CE (%)	Yield [4-15 keV] (J/sr)
1	3.7	0.11	1.5×2.2	1.0	moderate	2.5×10^{15}	10.9 ± 2.2	0.71	40.1 ± 8.8
2	3.7	0.11	2.0×2.2	1.0	mod. or wide	2.0-2.5×10^{15}	9.9 ± 3.9	0.66	26.5 ± 10.8
3	3.7	0.11	2.5×2.2	1.0	moderate	2.6×10^{15}	10.3 ± 2.7	0.67	25.4 ± 7.5
4	3.5	0.11	1.5×1.2	1.0	moderate	7.9×10^{15}	3.5 ± 1.8	0.22	16.1 ± 14.6
5	4.8	0.15	1.5×1.2	1.2	tight	5.6-6.5×10^{16}	6.3 ± 2.8	0.43	15.4 ± 7.1
6	6.5	0.20	1.5×1.2	1.2	tight	5.5-6.2×10^{16}	3.1 ± 0.7	0.21	12.3 ± 2.5
7	3.3	0.10	0.9×2.0	3.0	moderate	4.5×10^{15}	3.3 ± 0.7	0.24	12.3 ± 2.5
8	3.7	0.11	2.0×2.2	3.0	moderate	2.6×10^{15}	5.5 ± 1.9	0.37	24.1 ± 17.0
9	3.5	0.11	2.0×2.2	1.0	moderate	8.4×10^{15}	7.4 ± 1.5	0.47	34.8 ± 20.8
10	4.6	0.14	2.0×2.2	1.0	moderate	8.3×10^{15}	9.1 ± 1.8	0.60	40.8 ± 24.3
11	3.5	0.11	2.0×2.2	3.0	wide	6.9×10^{14}	4.8 ± 1.0	0.31	31.8 ± 21.7

TABLE II: A summary of the high-energy X-ray yields from the targets shot in this series of experiments. Columns are the target type, aerogel density (ρ), the ratio of plasma-electron to laser-critical density (n_e/n_{cr}), the target dimensions (ID × length), laser pulse length, the laser focus (see Table I), laser intensity, the X-ray yield between 9–15 keV with uncertainty, the CE (assuming isotropic emission) in the 9–15 keV band, and the X-ray yield between 4–15 keV with uncertainty.

Type	ρ (mg/cm^3)	n_e/n_{cr}	target size (mm×mm)	pulse length (ns)	focus	I_L (W/cm^2)	Yield [0.03-3.5 keV] (J/sr)	CE (%)
1	3.7	0.11	1.5×2.2	1.0	moderate	2.5×10^{15}	523.3 ± 78.6	34.3
2	3.7	0.11	2.0×2.2	1.0	mod. or wide	2.0-2.5×10^{15}	673.4 ± 150.7	44.9
3	3.7	0.11	2.5×2.2	1.0	moderate	2.6×10^{15}	693.8 ± 175.0	45.5
4	3.5	0.11	1.5×1.2	1.0	moderate	7.9×10^{15}	257.8 ± 43.6	16.5
5	4.8	0.15	1.5×1.2	1.2	tight	5.6-6.5×10^{16}	261.5 ± 141.7	18.1
6	6.5	0.20	1.5×1.2	1.2	tight	5.5-6.2×10^{16}	137.5 ± 26.0	9.6
7	3.3	0.10	0.9×2.0	3.0	moderate	4.5×10^{15}	no data	–
8	3.7	0.11	2.0×2.2	3.0	moderate	2.6×10^{15}	583.1 ± 123.5	39.2
9	3.5	0.11	2.0×2.2	1.0	moderate	8.4×10^{15}	755.4 ± 115.3	48.0
10	4.6	0.14	2.0×2.2	1.0	moderate	8.3×10^{15}	689.5 ± 103.4	44.3
11	3.5	0.11	2.0×2.2	3.0	wide	6.9×10^{14}	854.9 ± 175.6	55.5

TABLE III: A summary of the high-energy X-ray yields from the targets shot in this series of experiments. Columns are the target type, the aerogel density (ρ), the ratio of plasma-electron to laser-critical density (n_e/n_{cr}), the target dimensions (ID × length), laser pulse length, the laser focus (see Table I), laser intensity, laser intensity, the X-ray yield per steradian between 0.03–3.5 keV with uncertainty, and the CE (assuming isotropic emission).

$\approx 3.7\,\mathrm{mg/cm^3}$, cylinder sizes of 2.0×2.2 mm inner diameter by length (i.e., volume of $6.9\,\mathrm{mm^3}$), laser intensities $\approx 2\times10^{15}\,\mathrm{W/cm^2}$ with a 1 ns square laser pulse, the maximum and minimum yields measured with the HENWAY spectrometer in the 9–15 keV band differ by $\approx \pm55\%$ around the average over that set of targets. However, the soft X-ray yields in the spectral range below 3.5 keV differ by only $\pm$ 13% around the average. In the case of the fifth point (inverted red triangle), which is for targets with aerogel densities $\approx 4.8\,\mathrm{mg/cm^3}$, cylinder sizes of 1.5×1.2 mm inner diameter by length, laser intensities $\approx 6\times10^{16}\,\mathrm{W/cm^2}$ with a 1.0–1.2 ns laser pulse, there is a single outlying point out of a total of four that introduces a large statistical variation in the data set. By contrast, for the first point in Figs. 7 and 8 (magenta circle), which is for targets with aerogel densities $\approx 3.7\,\mathrm{mg/cm^3}$, cylinder sizes of 1.5×2.2 mm ID by length (i.e., volume $3.9\,\mathrm{mm^3}$), laser intensities $\approx 2.5\times10^{15}\,\mathrm{W/cm^2}$ with a 1 ns square laser pulse, the HENWAY-derived yields in the 9–15 keV band vary by only $\approx \pm3\%$ around the average value, and the soft X-ray yields (Fig. 8) vary by less than 1% around the average for this target type. In this case, the uncertainty values in Tables II and III are dominated by the uncertainty in the instrumental response functions.

We have taken some of the data points from Fig. 7 and plotted them versus key target-design parameters such as plasma-electron density, target volume and laser intensity in Figure 9. These data points represent target yield in the 9–15 keV X-ray energy band averaged over all targets of a given type. The upper panel in Fig. 9 captures the behavior of the targets as a function of electron density (given as a fraction of the laser's critical density). The two points for type 2 and 3 targets nearly overlay each other, both with densities near $0.1\mathrm{n}_{cr}$. The data appear to show a trend of target yield (equivalently, conversion efficiency) decreasing as the target density increases from $0.1\mathrm{n}_{cr}$. However, it must be pointed out that the two higher-density target types (types 5 and 6) had smaller volumes and were shot at higher laser intensities than the three lower-density target types in the upper panel of Fig. 9. It appears from these shots that the optimal target density is one for which the plasma electron density is near 0.1–$0.12\mathrm{n}_{cr}$.

The middle panel of Fig. 9 compares the yields from targets that differ principally in initial cylinder volume. One can see that for the type 1, 2 and 3 targets, which have identical aerogel densities, hence similar plasma electron densities for similar laser intensities, that the resulting 9–15 keV X-ray yields are nearly independent of target volume. Also in the middle panel of Fig. 9 are three points representing targets with smaller volume than the type 1, 2 and 3 targets. While these types of targets were shot at moderate (types 4 and 7) to much (type 5) higher laser intensities than the type 1, 2 and 3 targets, laser intensity seems to have a modest effect on the yield (see below), and we conclude that for maximizing X-ray output for $h\nu > 9$ keV, a minimum target

volume of ≈ 4 mm^3 is required and that the 9–15 keV yield is essentially independent of target volume above this threshold.

The bottom panel of Fig. 9 displays yields for a number of target types as a function of laser intensity. The type 11, 2 and 9 targets all have similar aerogel densities and target volumes. As a result, it appears that the yield for the type 2 target is a maximum, and that the optimal laser energy for producing 9–15 keV X-rays from Ge-doped aerogels is in the range 2.0–$2.5\times10^{15}\,\mathrm{W/cm^2}$. The type 10 target also has a similar volume, but has a higher aerogel density. The yield from the type 10 target is higher than the type 9 target, meaning that the higher intensity may be better matched to the higher aerogel density, but the optimal yield still occurs for the intensities used to drive the type 2 targets. The type 8 target shown in the figure had similar volume and aerogel density as the optimal type 2 target. However, the type 8 target was shot with a 3 ns laser pulse (Fig. 1), with the beam focusing adjusted to give the same intensity on target as for the 1 ns pulses used for the type 2 targets. The lower laser power in the 3 ns pulses (target types 8 and 11) seems to lead to lower yields, regardless of the actual laser intensity on target. The type 4 and 5 targets in the bottom panel of Fig. 9 had smaller volumes than the other target types in the figure. In this case, higher temperatures that result from the higher laser intensities and smaller volumes may actually have enhanced the 9–15 keV X-ray yields from these targets, but it is impossible to quantify this effect.

The yields for the type 1, 2 and 3 targets stand above the others in Fig. 7, despite the large error bars on the second point. These points represent the 9–15 keV X-ray yield from targets all of which have densities in the range $\rho = 3.6$–$3.7\,\mathrm{mg/cm^3}$, 1 ns laser pulses, laser intensities in the range 2.0–$2.6\times10^{15}\,\mathrm{W/cm^2}$. All the targets were shot with 18.7 ± 0.7 kJ of laser energy, and the measured yields indicate a CE of $0.7\pm0.24\%$ into X rays in the 9–15 keV band for all three target types. (Aside: the presence of the H-like Ge^{31+} line at ≈ 10.6 keV is only clearly seen in the spectra (see III A 1) from the smaller targets, which indicates that the smaller volume of these targets leads to higher temperatures, which, for the limited energy available at OMEGA may be beneficial to enhancing $h\nu > 9$ keV X-ray yields.)

Previous work by Workman and Kyrala [8, 31] has measured the CE of laser energy into X rays for solid Ge targets at the OMEGA laser. The results in Ref. [31] show a peak in the Ge CE at a laser intensity of 4×10^{16} W/cm^2, which is more than an order of magnitude above the optimal intensity found in the present work. However, the laser-absorption mechanisms and plasma-emission processes are probably quite different between the thin-foil targets in Refs. [8, 31] and the doped aerogels of the present work. They reported CE of 0.21% for the He_α ($1s^2 - 1s2p\ ^1P$) emission line of Ge^{30+} at a photon energy of 10.3 ± 0.275 keV. We find an average CE of $0.57\pm0.19\%$ for this same transition over the same en-
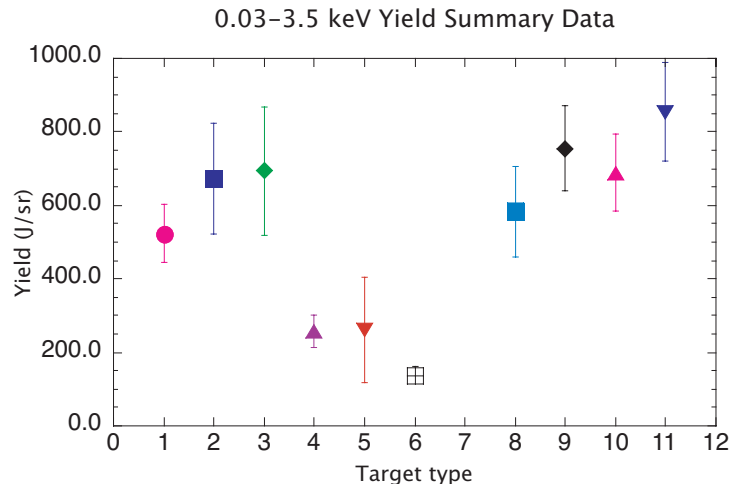
0.03–3.5 keV Yield Summary Data

FIG. 8: Yield data summary (in J/sr) for Ge-doped aerogels in the 0.03–3.5 keV band. The symbols in the figure represent the target types described in Table III, with the symbols from left to right corresponding to the entries going down the table. Note, there is no entry for the seventh target type.

ergy band in the output of the first three target types in Table II. Similarly, the X-ray conversion efficiency measurements for pre-exploded Ge-foils recently published [19] report a 1% CE in the Ge K-shell range for shots without pre-pulse and 3% CE for pre-exploded foils. Our results in this same spectral band average $0.7\pm0.24\%$ CE.

Many of the trends observed above for the points in Fig. 9 apply for the output from our Ge-doped aerogel targets in the softer (0.03–3.5 keV) energy range (Figure 10). However, the trend in the measured yields is more strongly increasing with target volume (middle panel) in this softer energy band. This may be due to a correlation between larger target volumes and lower plasmas temperatures. Also, one thing that does stand out is that the soft X-ray emission from the eleventh target type, which was shot with $I_L \approx 6\times10^{14}$ W/cm^2, is very strongly enhanced (lower panel). Given that the lower intensity corresponds to a lower plasma-electron temperature, and that emission in this band includes Ge L-shell emission, Si and O K-shell emission (see Fig. 6), the enhancement is not surprising if, in fact, higher plasma temperatures are burning out the lower-charged ions that dominate emission in this band.

B. X-Ray Waveforms

The X-ray diodes in the DMX and DANTE diagnostics, as well as the SNL PCDs and additional PCDs fielded by LLNL measure the temporal waveform of the X-rays emitted from our doped-aerogel targets. The detectors can be filtered to give the X-ray waveforms in different spectral bands; the $h\nu > 4$ keV waveforms presented here were measured with PCDs filtered with 254 μm of Kapton and 15.6 μm of Al. Figure 11 shows

the X-ray waveforms for emission above 4 keV from three of our target types. As a general rule, the X-ray output in this higher-energy regime closely follows the laser power, with the leading edge of the X-ray pulse lagging the leading edge of the laser power. This lag is due to the finite time required to heat and ionize the target to a regime where Ge K-shell emission is produced. The top panel in Fig. 11 shows characteristic X-ray waveforms for $h\nu > 4$ keV for a one ns square laser pulse (39156) and for a 1.2 ns quasi-Guassian laser pulse (39157), both type-5 targets. For most targets driven with 1 ns square or quasi-Gaussian laser pulses, the X-ray power rises from 10 to 90% of its maximum in $\lesssim$ 700 ps and has a Guassian shape with an $\approx$ 1 ns full width at half maximum (FWHM). The fast characteristics of the X-ray waveform mean that high-bandwidth recording devices and compensation for bandwidth losses in the measured signals from long signal-cable runs are required [30]. However, even though the majority of X-ray pulses in the $h\nu > 4$ keV energy range follow the laser power quite closely (9 out of 14 one-ns shots behave similarly to the top panel in Fig. 11) there is also variation in the shape of the X-ray waveforms. The lower panel in Fig. 11 shows one such result, where for shot number 44158 (a type-2 target) there is a late time spike in the X-ray power nearly a full nanosecond after the end of the laser pulse (5 out of 14 comparable shots demonstrate late-time phenomena). This behavior is confirmed on all complimentary diagnostics each time that it occurred. The late-time enhancement of the X-ray power in shot 44158 is due to hydrodynamic motion of the Be cylinder wall toward the cylinder axis, which results in a high-density emitting region in the shape of a jet (see § III C). This phenomenon, and the resulting spike in the X-ray emission from the target is seen in two-dimensional radiation-hydrodynamic
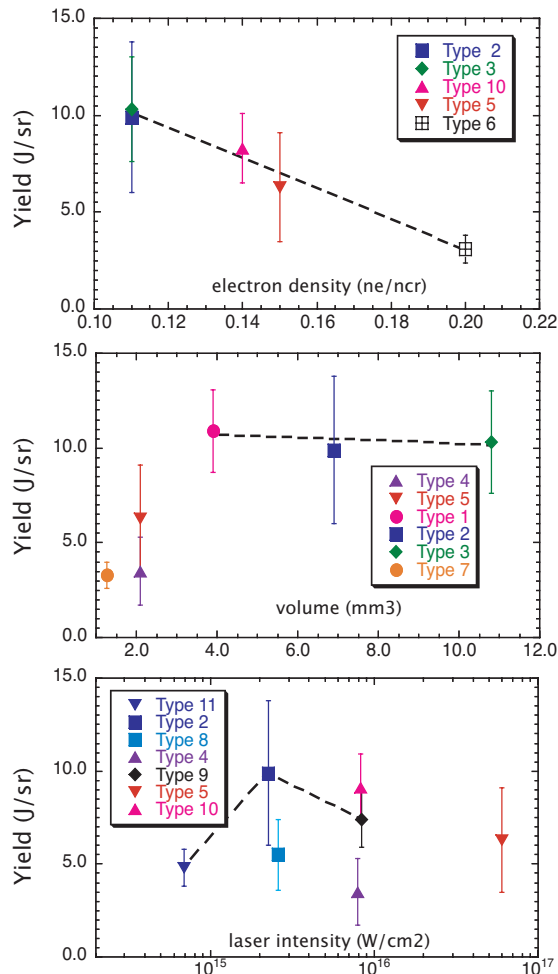
FIG. 9: (top) X-ray yield numbers for the Ge K-shell (9–15 keV) band for five target types (Table II) as a function of plasma electron density. (middle) X-ray yield numbers for the Ge K-shell band for six target types as a function of initial target volume. (bottom) X-ray yield numbers for the Ge K-shell band from seven target types as a function of laser intensity. The dashed lines in each panel are fits to (some of) the data that have been done simply to guide the eye.
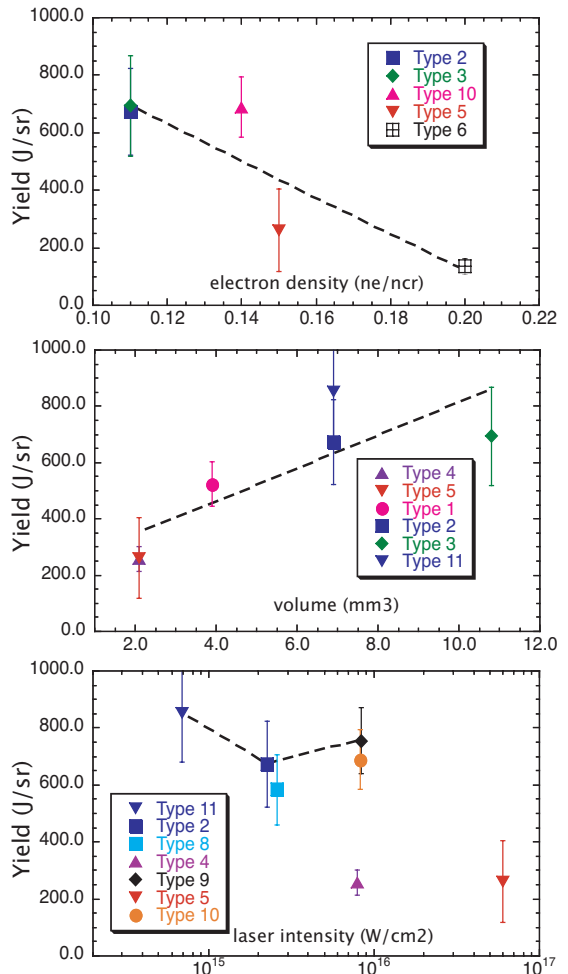
FIG. 10: (top) X-ray yield numbers for the 0.03–3.5 keV band for five target types (Table III) as a function of plasma electron density. (middle) X-ray yield numbers for the 0.03–3.5 keV band for six target types as a function of initial target volume. (bottom) X-ray yield numbers for the 0.03–3.5 keV band from seven target types as a function of laser intensity. The dashed lines in each panel are fits to (some of) the data that have been done simply to guide the eye.

simulations [32].

For the 3 ns pulses (e.g., shot no. 44157, a type-8 target, in Fig. 11), the X-ray waveforms show peaks in the X-ray signals after the peak of the laser power that are nearly simultaneous with the third plateau in the laser power, which corresponds to the firing of the low-angle cone 1 beams. The additional lag in the X-ray-power rise with respect to the laser power is due to a slower plasma-heating rate for the 3 ns laser shots. The result of using the 3 ns laser drive shown in Fig. 11 is a X-ray power profile in the $h\nu > 4$ keV band that can be fit with a Gaussian shape with a FWHM of ≈ 1.6 ns and with a relaxed rising edge compared to the X-ray power from a

1 ns-driven target.

Since we are examining the X-ray yield from the target in different spectral bands (cf. Tables II and III), it is appropriate to point out that the temporal history of the X-ray power emitted in different bands is different. Figure 12 compares the measured $h\nu > 4$ keV X-ray power with the X-ray power measured with a PCD that was filtered with only 8 μm Kapton. This channel in the PCD array was sensitive to all X rays with energies greater than 1 keV. It can be seen from the figure that for the shot displayed (51167, a type 2 target), the softer X-ray response has a FWHM that is $\approx 60\%$ wider than for the $h\nu > 4$ keV waveform. In general, the X-ray waveforms
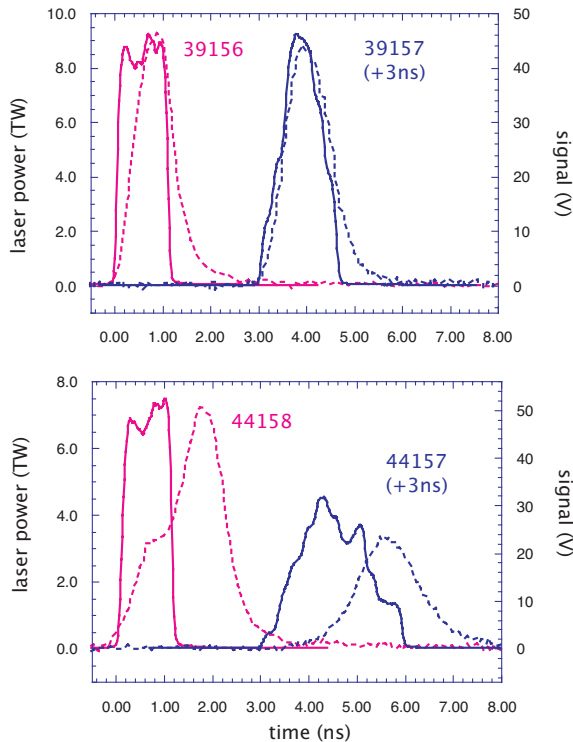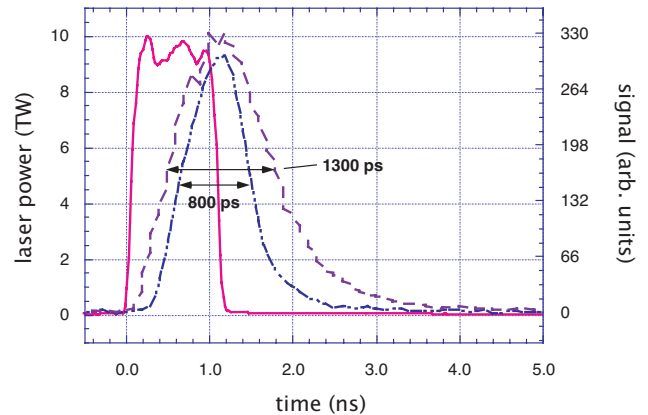
FIG. 12: Laser power (solid, left scale) and measured X-ray power for $h\nu > 4$ keV (dash-dot, right scale) and for $h\nu > 1$ keV (dashed, right scale) for shot 51167, a type-2 target.

FIG. 11: Laser power (solid, left scale) and PCD-measured X-ray power (dashed, right scale) for (top) two ρ=4.8 mg/cm^3 targets in small (1.5×1.2 mm [ID×L]) cylinders ($I_L = 6.5×10^{16}$ and $5.6×10^{16}$ W/cm^2 for shots 39156 and 39157, respectively) and (bottom) laser power (solid) and PCD-measured X-ray power (dashed, right scale) for two 3.7 mg/cm^3 targets in large (2.0×2.2 mm [ID×L]) cylinders ($I_L = 1.9×10^{15}$ and $2.6×10^{15}$ W/cm^2 for shots 44158 and 44157, respectively).

measured with the 8 μm Kapton channel in the PCD array ranged from 40–60% greater in duration than the $h\nu > 4$ keV waveforms.

C. Two-Dimensional X-ray Imaging

In order to measure the extent and history of the laser heating, a X-ray framing camera was fielded nearly perpendicular to the axis of the cylindrical target. The camera was filtered with 406 μm of Be, which lets through X rays with energies greater than 3 keV. The camera has an array of 16 50-μm pinholes in front, which are imaged onto four strips of a microchannel plate (MCP) detector. The camera and detector were rotated in order to have the axis of the MCP strips parallel to the axis of the cylinder holding the doped aerogel. The camera had either a 4× or a 2× magnification, the former of which would fit the 1.5 mm diameter aerogel targets (types 1, 4–6) onto the 7 mm width of the MCP strips of the XRFC, while images at the latter magnification filled the strips for

the larger-sized targets. Five images from shots 39154 ($\rho = 4.8$ mg/cm^3, 1.5 × 1.2 mm [ID×L], type 5) and 46616 ($\rho =3.7$ mg/cm^3, 1.5 × 2.2 mm [ID×L], type 1) are shown in Fig. 13. The images in Fig. 13 show that the aerogel heats quickly in the radial direction, which is closer to the direction of propagation of the steeper-angle beam cones, and that at approximately 750 ps the heat fronts from the two faces of the cylinder meet in the axial direction in both cases, despite the longer length of the target in shot 46616. The $h\nu > 4$ keV X-ray waveform from the target in shot 46616, which had a 1 ns square laser pulse, has the late-time behavior as seen in Fig. 14 that includes an enhancement of the emitted X-ray power that corresponds to the time of the axial stagnation seen in the 1500 ps frame in Fig. 13. The X-ray waveform for shot 39154 tracks the laser power very closely (nearly identically to shot 39156 in Fig. 11). All the cases of targets that demonstrate late-time hard-X-ray emission that does not follow the laser-power waveform demonstrate the formation of a jet-like feature like that seen in the images in Fig. 13 for shot 46616.

Figure 15 shows a time-integrated X-ray pinhole camera image of the X-ray emission ($h\nu > 3$ keV) from the type-2 target used in shot 44158. The camera was filtered with 254 μm of Be and 12 μm of Al, with a 11 μm diameter pinhole, it imaged the target onto a charge-injection device (CID) with a 4× magnification. The laser power and the measured hard-X-ray ($h\nu > 4$ keV) waveform for this target are shown in Fig. 11. Unlike the late-time shoulder on the X-ray power for shot 46616 discussed above, the peak X-ray emission for shot 44158 is observed to occur a full ns after the end of the laser pulse. Although the image in Fig. 15 is time integrated and cannot reveal the unique history of the laser heating of this target, the obvious effect of the radial compression due to wall motion is seen in the bright emitting region
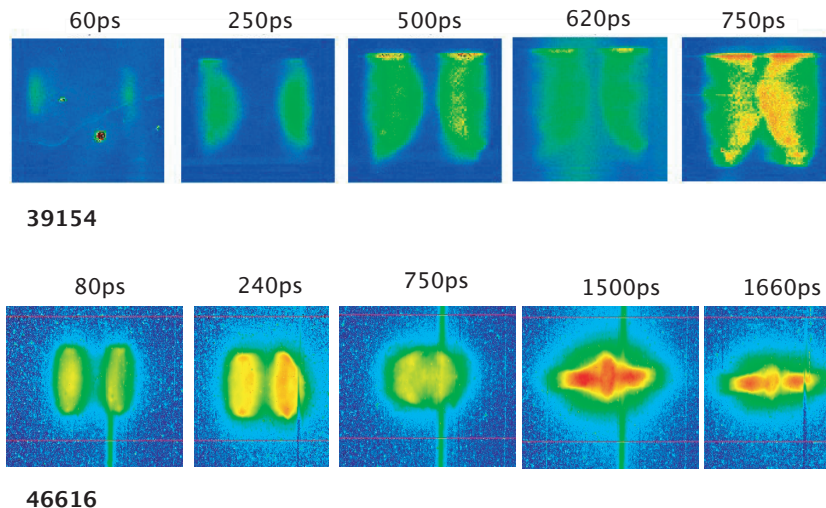
FIG. 13: XRFC images for shots 39154 and 46616. Both targets demonstrate the overlap of the heated X-ray regions from the open ends of the cylinders, but the target for 46616 shows the formation of a late-time jet of plasma on axis due to compression from cylinder-wall material that has stagnated on the axis.
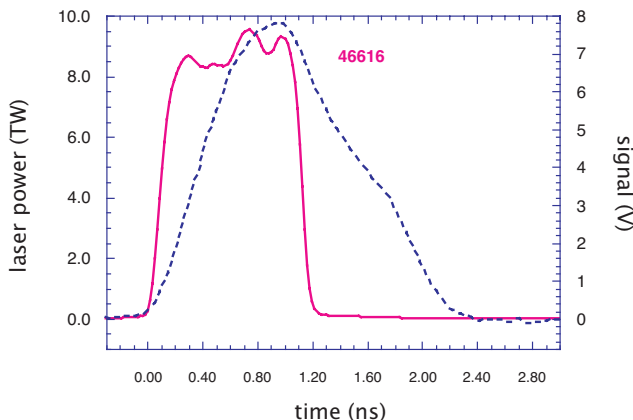

FIG. 14: Laser power (solid, left scale) and measured X-ray power for $h\nu > 4$ keV (dashed, right scale) for shot 46616, a type-1 target.

along the target's axis.

Geometrical analysis of the beam propagation for the laser pointing depicted in Fig. 1 reveals that the cone 1, 2 and 3 beams have path lengths through the aerogel medium to the cylinder wall of 1557, 1494 and 1168 μm, respectively for Be cylinders with a 2.0 mm IDs, and 872, 1121, and 876 μm, respectively, for Be cylinders with 1.5 mm IDs. The principal method by which laser energy is deposited in the medium is inverse bremsstrahlung (IB) absorption. The IB absorption length in the plasma is given in centimeters by [33]

$$\lambda_{IB} = \frac{0.56\lambda_L^2 T_e^{3/2}}{(n_e/n_{cr})^2 Z ln\Lambda} \left(1 - \frac{n_e}{n_{cr}}\right)^{1/2} \qquad (2)$$

where λ_L is the laser wavelength in μm, T_e is the plasma electron temperature in keV, Z is the average charge state in the plasma and $ln\Lambda$ is the Coulomb logarithm. Using Eq. 2, with $Z =< Z >$ as given in § II B, with T_e as found by fitting the continua in the HENWAY data (e.g., Fig. 2) and the value of n_e/n_{cr} from Eq. 1, one finds values of $\lambda_{IB} \approx 1212$–$1220$ μm for the smaller-inner-diameter, $\rho = 4.8$ mg/cm^3 (type 5) targets in the upper panel of Fig. 11 (shots 39156 and 39157), ≈ 2000 μm for the larger-inner-diameter, $\rho = 3.6$ mg/cm^3 (type 2) target of shot 42750 (which has a X-ray waveform like those of 39156 and 39157), and ≈ 2690 μm for the $\rho = 3.7$ mg/cm^3 (type 2) target in shot 44158, which is the broader X-ray pulse in the bottom panel of Fig. 11. In all cases, this simple estimate would suggest that the the laser beams reach the walls of the Be cylinder with a non-negligible fraction of their total energy remaining. Clearly, there are short comings with this static picture of laser absorption - the temperature in the plasma is not fixed, and the electron density along the laser path changes locally in response to the plasma heating. However, it is instructive that all the shots that have the broader X-ray waveform (like 44158 and 46616 in Figs. 11 and 14) exhibit the kind of strong on-axis jet seen in Figs. 13 and 15, and that those shots also have some of the longer IB absorption lengths (mainly due to having the highest T_e's) of all the shots studied here.

D. Laser Scattering

Long scale length, underdense plasmas, which are exactly the kind of plasmas our aerogel targets become, can reflect significant amounts of a laser's energy [33, 34]. The two instability channels by which the long scale
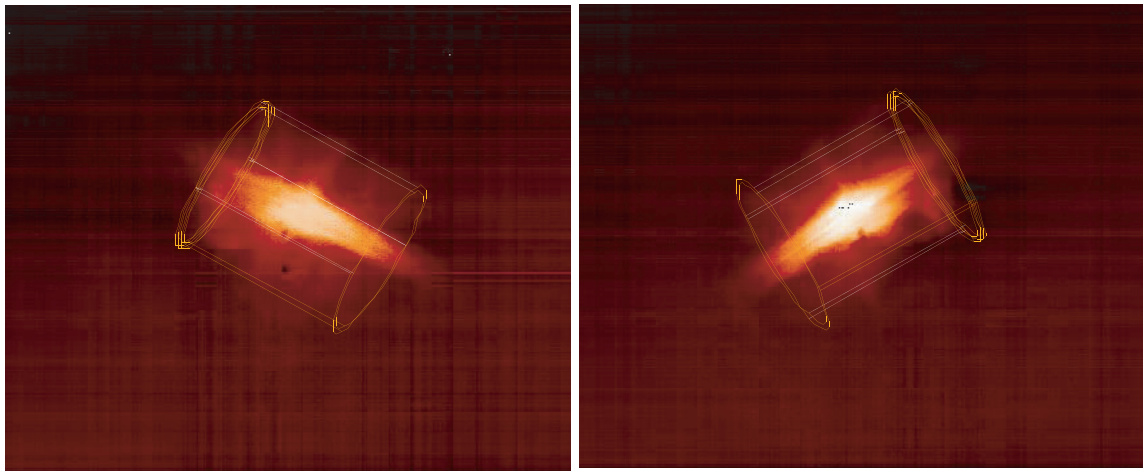
FIG. 15: Time-integrated X-ray pinhole camera images of the type-2 target used on shot 44158. The cameras (H13 left, H3 right) had nearly side-on views of the target. The emission is dominated by a collimated region along the target's axis that we hypothesize is due to radial compression of the hot plasma. A wireframe drawing of the targets pre-shot outline as viewed by the camera has been placed on each image

length, underdense plasma may reflect laser energy are by stimulated Brillouin scattering (SBS) or stimulated Raman scattering (SRS) [35]. We have measured the energy backscattered from our targets back into the optics of one cone 2 and one cone 3 beam (beams 25 and 30, respectively). The Full Aperture Backscatter System (FABS) [36], which employs a calibrated calorimeter, measured the reflected energy for those two beams, the results for the 11 types of targets discussed above are shown in Fig. 16. The steeper incidence angle of the cone 3 beam means that the backscattered fraction of beam energy is larger than for the cone 2 beam (assuming that the laser propagation direction is at an angle relative to a density gradient in the target that is oriented along the target's axis [35]). In our data we find that the cone 3 SRS signals are an average of $5\times$ larger than the corresponding cone 2 signals, and for the SBS channel an average of $1.6\times$ larger. The points in Fig. 16 represent the fraction of total laser energy scattered in both the SRS and SBS channels measured for cone 2 and 3 beams, and an estimated contribution for the cone 1 beams. Since we do not have a measurement of backscatter for the cone 1 beams, we have assumed the scattering losses in the SRS and SBS channels are the same as those measured for the cone 2 beams. Since the scattering losses decrease as the beam-cone angle decreases, this assumption means that the points in Fig. 16 are upper bounds on energy reflected from each target type. Scattering losses are small, between 5–7% for most of our targets, and much less for the targets with the highest yields in the 9–15 keV X-ray band. We have examined images of reflective plates around the optics for the beams in question and have found minimal energy scattered outside of the collection optics. The CE's in Tables II and III are given relative to the total energy delivered to the target, and have *not* been adjusted to account for only energy absorbed in the

target.

IV.   SUMMARY AND CONCLUSION

We recommend Ge-doped aerogel targets fabricated such that $n_e = 0.1$–$0.12 n_{cr}$ ($\rho = 3.6$–4.1 mg/cm^3 for the materials described here), shot at laser intensities of $I_L = 2.0$–2.6×10^{15} W/cm^2. This will yield 10.1 ± 3.5 J/sr of X rays with energies above 9 keV (averaging over type 1, 2 and 3 targets), or, equivalently, 127 ± 44 J/sphere assuming isotropic emission, and 678 ± 157 J/sr for energies below 3.5 keV for 1 ns laser pulses (averaging over type 2 and 3 targets only). The X-ray spectra are dominated by the 10.3 keV Ge^{30+} He$_\alpha$ line in the hard band and by Ge L-shell emission and Si and O K-shell emission in the soft band. These results suggest a conversion efficiency of $\approx 0.7\%$ for isotropic emission in the harder spectral band, which is below the $\approx 3\%$ emitted into 4π quoted for recent work with pre-exploded Ge foils, and $\approx 45\%$ for isotropic emission in the soft X-ray band, which is consistent with measurements from gas targets. There is a large X-ray continuum that makes up more than half the X-ray output from the targets in the range between 4 and 15 keV; the average emission-weighted spectral energy in this range is 7.1 keV. The overall laser energy lost by scattering from laser-plasma instabilities is seen to be $\lesssim 5$–7% from these targets, and more like 2–3% for the preferred type 2 and 3 targets. Generally, the X-ray flux from these targets follows the laser power delivered to the target with finite time lags necessary to achieve the required ionization and eventual radiative cooling of the plasma. However, for about 1/3 of the targets we have studied, the hard X-ray output shows strong to very strong late-time features that are correlated with strong enhancement of on-axis emission due to radial hydrody-
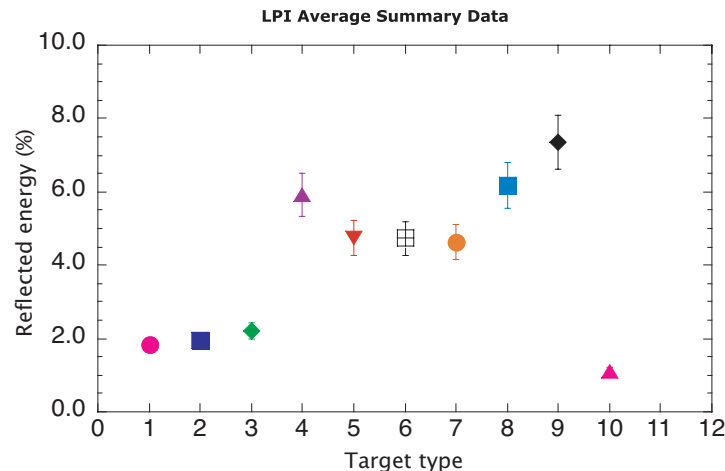
FIG. 16: Summary of the sum of SRS and SBS scattered energy for each target type in the present work. The SRS and SBS values for each shot are averaged over the measurement from a cone 2 and a cone 3 beam and an assumed (small) contribution for losses from the cone 1 beams and are expressed as a fraction of the total energy delivered.

namic compression of these plasmas. We can not explain why some targets on some shots form these axial jets and others do not. The duration soft X-ray flux is always significantly longer than the laser pulse.

Acknowledgments

[1] B. E. Blue, S. V. Weber, S. G. Glendinning, N. E. Lanier, D. T. Woods, M. J. Bono, S. N. Dixit, C. A. Haynam, J. P. Holder, D. H. Kalantar, et al., Physical Review Letters **94**, 095005 (pages 4) (2005).

[2] O. L. Landen et al., Eur. Phys. J. D **44**, 273 (2007).

[3] E. I. Moses, R. E. Bonanno, C. A. Haynam, R. L. Kauffman, B. J. MacGowan, and R. W. Patterson Jr, Eur. Phys. J. D **44**, 215 (2007).

[4] C. A. Haynam, P. J. Wegner, J. M. Auerbach, M. W. Bowers, S. N. Dixit, G. V. Erbert, G. M. Heestand, M. A. Henesian, M. R. Hermann, K. S. Jancaitis, et al., Applied Optics **46**, 3276 (2007).

[5] D. Besnard, Eur. Phys. J. D **44**, 207 (2007).

[6] O. L. Landen, D. R. Farley, S. G. Glendinning, L. M. Logory, P. M. Bell, J. A. Koch, F. D. Lee, D. K. Bradley, D. H. Kalantar, C. A. Back, et al., Rev. Sci. Instru. **72**, 627 (2001).

[7] R. Kauffman, in *Handbook of Plasma Physics; Vol. 3 Physics of Laser Plasmas*, edited by A. M. Rubenchik and S. Witkowski (Elsevier Science, North Holland, Amsterdam, 1991), pp. 111–162.

[8] J. Workman and G. A. Kyrala, Rev. Sci. Instru. **72**, 678 (2001).

[9] C. A. Back, J. Grun, C. Decker, L. J. Suter, J. Davis, O. L. Landen, R. Wallace, W. W. Hsing, J. M. Laming, U. Feldman, et al., Phys. Rev. Lett. **87**, 275003 (2001).

[10] K. B. Fournier, C. Constantin, C. A. Back, L. Suter, H.-K. Chung, M. C. Miller, D. H. Froula, G. Gregori, S. H. Glenzer, and O. L. Landen, J. Quant. Spect. and Rad. Transf. **99**, 186 (2006).

[11] C. A. Back, J. Davis, J. Grun, L. J. Suter, O. L. Landen, W. W. Hsing, and M. C. Miller, Physics of Plasmas **10**, 2047 (2003).

[12] K. B. Fournier, C. Constantin, J. Poco, M. C. Miller, C. A. Back, L. J. Suter, J. Satcher, J. Davis, and J. Grun, Phys. Rev. Lett. **92**, 165005 (2004).

[13] J. Denavit and D. W. Phillion, Physics of Plasmas **1**, 1971 (1994).

[14] C. J. Brinker and G. W. Scherer, *Sol-Gel Science: The Physics and Chemistry of Sol-Gel Processing* (Academic Press, San Diego, 1990).

[15] B. J. Clapsaddle, D. W. Sprehn, A. E. Gash, J. H. Satcher

Jr., and R. L. Simpson, J. Non-Cryst. Solids **350**, 173 (2004).

[16] C. Constantin, C. A. Back, K. B. Fournier, G. Gregori, O. L. Landen, S. H. Glenzer, E. L. Dewald, and M. C. Miller, Physics of Plasmas **12**, 063104 (pages 8) (2005).

[17] M. Tanabe, H. Nishimura, S. Fujioka, K. Nagai, N. Yamamoto, Z. Gu, C. Pan, F. Girard, M. Primout, B. Villette, D. Brebion, K. B. Fournier, A. Fujishima, and K. Mima, Applied Physics Letters **93**, 051505 (pages 5) (2008).

[18] F. Girard, J. P. Jadaud, M. Naudy, B. Villette, D. Babonneau, M. Primout, M. C. Miller, R. L. Kauffman, L. J. Suter, J. Grun, et al., Physics of Plasmas **12**, 092705 (pages 5) (2005).

[19] D. Babonneau, M. Primout, F. Girard, J. P. Jadaud, M. Naudy, B. Villette, S. Depierreux, C. Blancard, G. Faussurier, K. B. Fournier, L. Suter, R. Kauffman, S. Glenzer, M. C. Miller, J. Grün, J. Davis, et al., Physics of Plasmas **15**, 092702 (pages 15) (2008).

[20] K. B. Fournier, M. Tobin, J. F. Poco, K. Bradley, C. A. Coverdale, D. E. Beutler, T. V. III, S. B. Hansen, M. Severson, E. A. Smith, et al., in *Laser-Generated & Other Lab. X-ray & EUV Sources, Optics, Apps.*, edited by G. A. Kyrala, J.-C. Gauthier, C. A. MacDonald, and A. M. Khounsary (2005), vol. 5918 of *Proc. of SPIE*, pp. 5918N1–10.

[21] T. R. Boehly et al., Rev. Sci. Instru. **66**, 508 (1995).

[22] J. M. Soures, R. L. McCrory, C. P. Verdon, A. Babushkin, R. E. Bahr, T. R. Boehly, R. Boni, D. K. Bradley, D. L. Brown, R. S. Craxton, et al., Physics of Plasmas **3**, 2108 (1996).

[23] S. B. Hansen, private communication, 2008.

[24] The analysis was done by Galbraith Laboratories, Inc., see www.galbraith.com for details (URL last accessed on 2/3/2009).

[25] A more complete technical description and evaluation can be found at: http://www.jobinyvon.com/SiteResources/Data/MediaArchive/files/Emission/TN05.pdf (URL last accessed on 2/3/2009).

[26] L. N. Koppel and J. D. Eckels, Lawrence Livermore National Laboratory Report, UCRL-79781 (October, 1977).

[27] R. B. Spielman, Rev. Sci. Instr. **66**, 867 (1995).

[28] J. L. Bourgade, B. Villette, J. L. Bocher, J. Y. Boutin, S. Chiche, N. Dague, D. Gontier, J. P. Jadaud, B. Savale, R. Wrobel, et al., Rev. Sci. Instr. **72**, 1173 (2001).

[29] H. N. Kornblum, R. L. Kauffman, and J. A. Smith, Rev. Sci. Instr. **57**, 2179 (1986).

[30] K. B. Fournier, M. J. May, S. A. MacLaren, C. A. Coverdale, and J. F. Davis, Lawrence Livermore National Laboratory Report, UCRL-TR-224095-REV-1 (June, 2007).

[31] J. Workman and G. A. Kyrala, in *Applications of X Rays Generated from Lasers and Other Bright Sources II*, edited by G. A. Kyrala and J.-C. J. Gauthier (SPIE, 2001), vol. 4504 of *Proc. of SPIE*, pp. 168–179.

[32] K. B. Fournier, C. Constantin, G. Gregori, M. C. Miller, C. A. Back, L. J. Suter, J. Davis, and J. Grun, in *Atomic Processes in Plasmas*, edited by J. S. Cohen,S. Mazevet and D. P. Kilcrease (AIP, 2004), vol. 730, pp. 223–232.

[33] J. D. Lindl, *Inertial Confinement Fusion* (Springer-Verlag, New York, 1998).

[34] S. H. Glenzer, P. Arnold, G. Bardsley, R. L. Berger, G. Bonanno, T. Borger, D. Bower, M. Bowers, R. Bryant, S. Buckman, et al., Nuclear Fusion **44**, S185 (2004).

[35] W. L. Kruer, *The Physics of Laser Plasma Interactions* (Westview Press, Boulder, 2003).

[36] M. D. Wilke, J. C. Fernández, R. R. Berggren, R. F. Horton, D. S. Montgomery, J. A. Faulkner, L. D. Looney, J. R. Jimerson, Rev. Sci. Instrum. **68**, 672 (1997).